Article

SOURCE DATA | TRANSPARENT PROCESS | OPEN ACCESS

EMBO reports

Intra-epithelial non-canonical Activin A signaling safeguards prostate progenitor quiescence

Francesco Cambuli[1,2,*,†,‡], Veronica Foletto[1,†], Alessandro Alaimo[1], Dario De Felice[1], Francesco Gandolfi[3], Maria Dilia Palumbieri[1], Michela Zaffagni[1], Sacha Genovesi[1], Marco Lorenzoni[1], Martina Celotti[1], Emiliana Bertossio[1], Giosuè Mazzero[4], Arianna Bertossi[1], Alessandra Bisio[1], Francesco Berardinelli[5,6], Antonio Antoccia[5], Marco Gaspari[7], Mattia Barbareschi[4], Michelangelo Fiorentino[8], Michael M Shen[2], Massimo Loda[9], Alessandro Romanel[3] & Andrea Lunardi[1,**]

Abstract

The healthy prostate is a relatively quiescent tissue. Yet, prostate epithelium overgrowth is a common condition during aging, associated with urinary dysfunction and tumorigenesis. For over thirty years, TGF-β ligands have been known to induce cytostasis in a variety of epithelia, but the intracellular pathway mediating this signal in the prostate, and its relevance for quiescence, have remained elusive. Here, using mouse prostate organoids to model epithelial progenitors, we find that intra-epithelial non-canonical Activin A signaling inhibits cell proliferation in a Smad-independent manner. Mechanistically, Activin A triggers Tak1 and p38 MAPK activity, leading to p16 and p21 nuclear import. Spontaneous evasion from this quiescent state occurs upon prolonged culture, due to reduced Activin A secretion, a condition associated with DNA replication stress and aneuploidy. Organoids capable to escape quiescence *in vitro* are also able to implant with increased frequency into immunocompetent mice. This study demonstrates that non-canonical Activin A signaling safeguards epithelial quiescence in the healthy prostate, with potential implications for the understanding of cancer initiation, and the development of therapies targeting quiescent tumor progenitors.

Keywords Activin A; *MAP3K7*; organoids; prostate; TGF-β

Subject Categories Cancer; Signal Transduction; Stem Cells & Regenerative Medicine

DOI 10.15252/embr.202154049 | Received 24 September 2021 | Revised 22 February 2022 | Accepted 24 February 2022

EMBO Reports (2022) e54049

Introduction

The healthy prostate is a relatively quiescent tissue during adulthood (De Marzo *et al*, 1998; Toivanen & Shen, 2017). In contrast, the overgrowth of the prostatic epithelium is one of the most common conditions experienced by aging men, being linked with urinary dysfunction and tumorigenesis (Ørsted & Bojesen, 2013). The molecular mechanisms causing exit from quiescence are poorly understood. Chronic inflammation—potentially induced by infection (e.g., prostatitis) (Shinohara *et al*, 2013; Kwon *et al*, 2014; Simons *et al*, 2015), chemical damage (e.g., urine reflux) (Kirby *et al*, 1982), physical trauma (e.g., corpora amylacea) (DuPre *et al*, 2018), dietary carcinogens (Nakai *et al*, 2007), obesity (Kwon *et al*, 2016a), hormonal imbalance (e.g., low systemic androgen levels) (Zhang *et al*, 2016; Wang *et al*, 2017), and aging (Crowell *et al*, 2019)—has been implicated in DNA damage, oxidative stress, and atrophy, leading to a proliferative response (Sfanos *et al*, 2018; de Bono *et al*, 2020). Considering the high frequency of these events, it would be logical to hypothesize specialized mechanisms to safeguard epithelial quiescence, but they have been rarely investigated.

1 The Armenise-Harvard Laboratory of Cancer Biology & Genetics, Department of Cellular, Computational and Integrative Biology (CIBIO), University of Trento, Trento, Italy
2 Department of Medicine, Genetics and Development, Urology, Systems Biology, Herbert Irving Comprehensive Cancer Center, Columbia University Irving Medical Center, New York, NY, USA
3 Laboratory of Bioinformatics and Computational Genomics, Department of Cellular, Computational and Integrative Biology (CIBIO), University of Trento, Trento, Italy
4 Santa Chiara Hospital-APSS, Trento, Trento, Italy
5 Department of Science, University of Roma Tre, Roma, Italy
6 Laboratory of Neurodevelopment, Neurogenetics and Molecular Neurobiology Unit, IRCCS Santa Lucia Foundation, Roma, Italy
7 Department of Experimental and Clinical Medicine, University of Catanzaro, Catanzaro, Italy
8 Department of Experimental, Diagnostic and Specialty Medicine, University of Bologna, Bologna, Italy
9 Department of Pathology and Laboratory Medicine, Weill Medical College of Cornell University, New York, NY, USA
*Corresponding author. Tel: +1 646 888 3997; E-mail: cambulif@mskcc.org
**Corresponding author. Tel: +39 0461 285288; E-mail: andrea.lunardi@unitn.it
†These authors contributed equally to this work as first authors
‡Present address: Molecular Pharmacology Program, Sloan Kettering Institute, Memorial Sloan Kettering Cancer Center, New York, NY, USA

It has long been known that transforming growth factor β (TGF-β) signaling inhibits the proliferation of a large variety of epithelial cell types (Tucker *et al*, 1984; Moses *et al*, 2016), including those of the prostate (McKeehan & Adams, 1988). SMAD factors are the canonical intracellular mediators of this signaling, but additional non-canonical pathways can also be triggered by TGF-β receptors (Massagué, 2012; Derynck & Budi, 2019). In gastrointestinal (GI) carcinomas (e.g., pancreas, colon), the canonical pathway is frequently mutated (Bailey *et al*, 2016; Yaeger *et al*, 2018). However, outside of the GI tract, TGF-β/SMAD components are rarely inactivated in tumors, leaving unexplained the nature of the intracellular signaling responsible for the cytostatic effect of TGF-β (David & Massagué, 2018; Gerstung *et al*, 2020).

Enhanced Tgf-β signaling has been linked with the presence of quiescent epithelial progenitors in the proximal/periurethral region of the mouse prostate (Salm *et al*, 2005; Wei *et al*, 2019). Recent single-cell studies have confirmed the enrichment of a variety of epithelial progenitors—basal, luminal proximal (LumP), and periurethral (PrU) cells—in this anatomical district, though also present at low frequency in the distal compartment (Henry *et al*, 2018; Crowley *et al*, 2020; Guo *et al*, 2020; Joseph *et al*, 2020; Karthaus *et al*, 2020; Mevel *et al*, 2020). Such cells are known to be particularly quiescent during homeostasis (Pignon *et al*, 2015; Kwon *et al*, 2020), but also to exhibit extensive regenerative potential in *ex vivo* assays (Kwon *et al*, 2016b; Crowley *et al*, 2020).

Thus, the TGF-β-induced cytostatic response in epithelial progenitors may be relevant for the control of quiescence, but the complexity of this pathway, the lack of interpretable genetic alterations in patients, and the heterogeneous cellular composition of the prostate have so far hampered mechanistic investigations. Here, we reasoned that prostate organoid models (Chua *et al*, 2014; Karthaus *et al*, 2014)—in combination with orthotopic transplantation approaches—may provide a biologically relevant, and experimentally amenable, system for addressing this question.

Results

Mouse prostate organoid cultures enable the continuous expansion of epithelial progenitors in a near-physiological manner

Initially, we set out to assess whether mouse prostate organoids are a representative and informative model for the study of the prostate epithelium, in light of recent discoveries on prostate cellular heterogeneity and dynamics (Barros-Silva *et al*, 2018; Henry *et al*, 2018; Crowley *et al*, 2020; Guo *et al*, 2020; Karthaus *et al*, 2020; Kwon *et al*, 2020; Mevel *et al*, 2020). Considering our interest in signaling, we focused on a culture method in defined media conditions. This protocol relies on a mix of growth factors and inhibitors, including Egf, Noggin, R-spondin 1, the Tgf-β receptors inhibitor A83-01, and dihydrotestosterone (ENRAD) (Karthaus *et al*, 2014; Drost *et al*, 2016). We generated a biobank of mouse prostate organoids, starting from bulk populations of cells from distinct prostate lobes and mouse strains (Fig 1A, Appendix Fig S1A–E). In line with previous studies (Chua *et al*, 2014; Karthaus *et al*, 2014; Drost *et al*, 2016), we found that, upon tissue dissociation, only a small fraction of cells (approx. 1%) was capable to generate organoids in culture and that organoid-forming efficiency increased over passages, suggesting enrichment for epithelial progenitors (Fig 1B). To gain greater insights, we longitudinally tracked organoid formation—from single cells to fully formed organoids—and we observed a progressive expansion of cells expressing the progenitor epithelial surface antigen Sca-1 (encoded by *Ly6a*; Fig 1C) (Kwon *et al*, 2016b; Crowley *et al*, 2020). Thereafter, the level of Sca-1 appeared to be stable over a long culture period (e.g., 10 weeks). To extend our observations, we performed transcriptomic analyses on three organoid lines derived from distinct mouse prostate lobes (Fig 1D and E). Consistently with enrichment for epithelial progenitors, organoids expressed high levels of genes specific for the proximal and periurethral compartments (e.g., *Psca*, *Tacstd2*, and *Ly6d*), as well as basal (e.g., *Krt5*, *Krt14, Trp63*) and luminal marker genes (e.g., *Krt8*, *Ar, Foxa1*). In contrast, distal luminal markers were lowly expressed (e.g., *Nkx3.1*, *Pbsn*, *Sbp*). Histological (H&E) and immunofluorescent (IF) analyses confirmed that prostate organoids, for the most part, are made up of a bilayer of cuboidal cells, displaying progenitor marker proteins (e.g., Krt7, Ppp1r1b), and resembling the cyto-architecture of the periurethral/proximal compartment (Figs 1F–H and EV1A). As expected for periurethral/proximal cells—which are known to be castration resistant—mouse prostate organoids were reversibly dependent on androgen for lumen formation (Fig EV1B–D), but minimally for their survival (Fig EV1E).

The epithelium of the prostate is characterized by a slow cellular turnover. In contrast, prostate organoids appeared to proliferate indefinitely (Fig EV2A and B)—while retaining low levels of genomic instability (Fig EV2C and D)—raising the question of how culture conditions enable persistent cycling in a near-physiological manner. Either an excess of stimulatory cues in culture, or a lack of inhibitory ones—or both—may explain the shift from homeostatic quiescence *in vivo* to unrestrained mitotic activity *in vitro*. Using a "n -1 approach" for assessing the requirement for growth factors and inhibitors in culture (Fig EV3A), we found that prostate organoids are strictly dependent on exogenous Egf (Fig EV3B–D), as well as Tgf-β receptors inhibition by A83-01. Given the limited understanding of prostate quiescence, we focused on the requirement for the Tgf-β receptors inhibitor A83-01 for the continuous expansion of mouse prostate organoid cultures.

Intra-epithelial non-canonical Activin A signaling is a key mediator of the Tgf-β induced cytostatic response in mouse prostate organoids

Upon A83-01 withdrawal, organoids displayed a marked reduction in EdU incorporation within 24 h, demonstrating a cytostatic response in this model (Fig 2A, Appendix Fig S2A). A83-01 is a potent inhibitor of three type-I Tgf-β family receptors, and two of them—Acvr1b and Tgfbr1 (also known as Alk4 and Alk5)—together with their ligands—Activin A (encoded by the *Inhba* gene) and Tgfb1—were found expressed in prostate organoids (Appendix Fig S2B) and shown to play critical roles in the inhibition of cell cycle induced by A83-01 depletion (Appendix Fig S2C and D). Paracrine and autocrine ligand–receptor interactions have been demonstrated to negatively regulate epithelial proliferation (Sporn & Todaro, 1980; Tucker *et al*, 1984) leading us to investigate the release of Tgf-β ligands in organoid cultures. We employed a click-chemistry approach to enrich secreted proteins released in the culture medium, followed by mass spectrometry analysis (Eichelbaum *et al*, 2012). Over multiple experiments, we consistently recovered

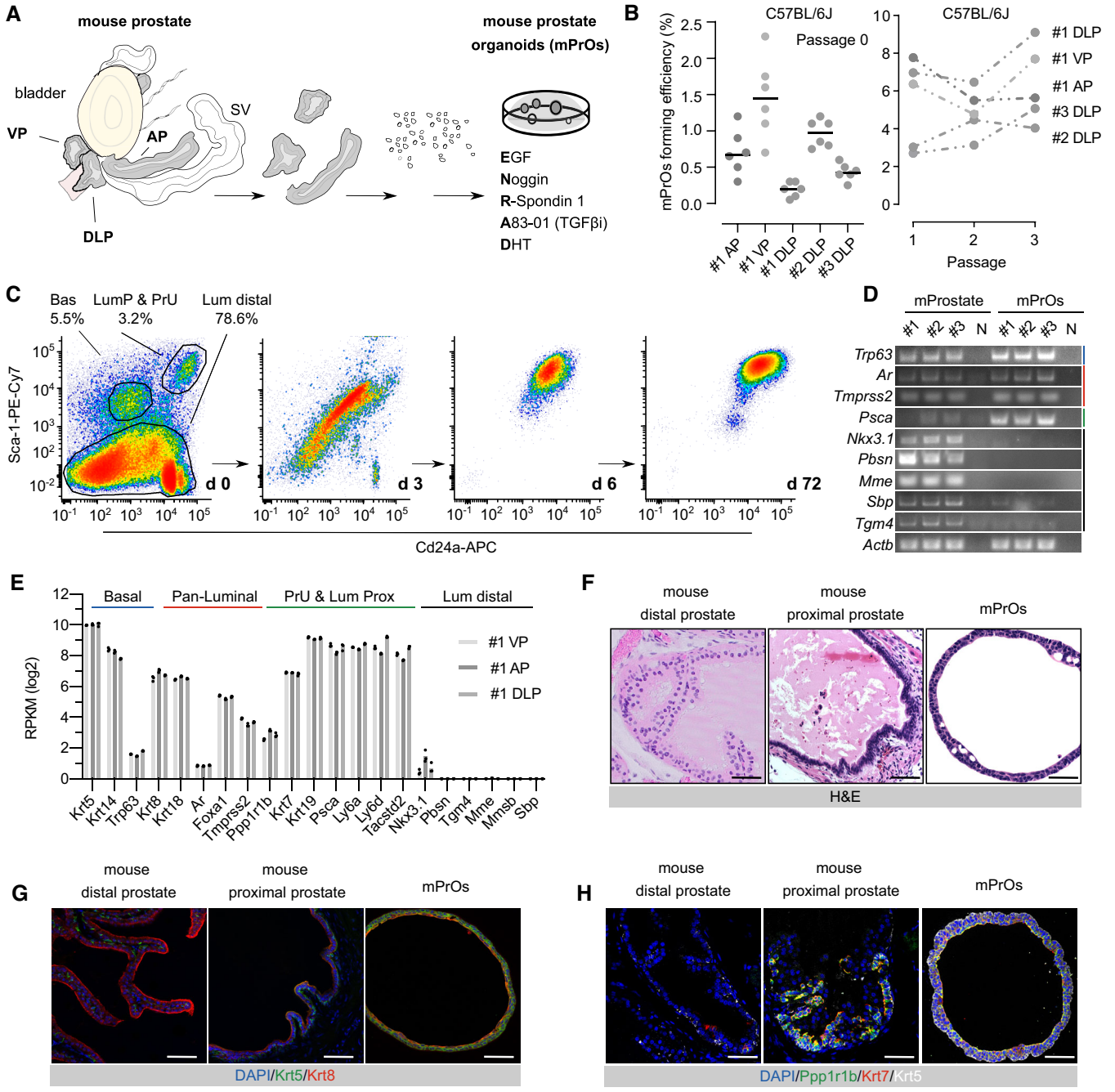

Figure 1. Mouse prostate organoids are highly enriched in epithelial progenitor cells.

A Schematic diagram describing organoid culture derivation (AP, Anterior Prostate; DLP, Dorso-Lateral Prostate; VP, Ventral Prostate; SV, Seminal Vesicle; DHT, dihydrotestosterone).

B Mouse prostate organoid forming efficiency. Efficiency at derivation (left; $n = 6$ biological replicates, data points are shown with crossing line representing mean value). Efficiency at passage 1-3 (right; $n \geq 3$ biological replicates per organoid line/passage; data are presented as mean).

C Representative longitudinal flow cytometry analysis of dissociated organoid cells (Bas, Basal; LumP, Luminal Proximal; PrU, Periurethral; Lum Distal, Luminal Distal).

D End-point RT–PCR analysis for selected marker genes ($n = 3$ biological replicates).

E Bulk-RNAseq analysis ($n = 3$ biological replicates; individual data points are shown with bar graphs representing mean value).

F Representative hematoxylin-eosin (H&E) staining of mouse prostate tissue and organoid sections (scale bars = 50 μm).

G Representative immunofluorescence (IF) analysis for selected markers in mouse prostate tissue and organoid sections (scale bars = 50 μm).

H IF staining for selected markers in mouse prostate tissue and organoid sections (scale bars = 50 μm).

Activin A peptides in the organoid supernatant, and only in one instance, a Tgfb1 peptide (Fig 2B). Western blot analysis of total organoids lysates confirmed the expression of Activin A in all the three lobe-specific organoid cultures, showing both monomeric and dimeric forms of the protein (Appendix Fig S2E). Of note, analysis of recently published single cell RNA sequencing datasets of adult mouse prostate (Data ref: Crowley *et al*, 2020) identified a small number of Basal, LumP, and PrU cells expressing *Inhba* (Appendix Fig S2F), while immunolocalization studies in mouse prostate tissue and organoid cultures detected Acvr1b in prostate progenitors (Fig 2C) with an expression pattern similar to Egfr (Fig EV3D). Replacement of A83-01 with Follistatin—a well-known Activin A inhibitor (Nakamura *et al*, 1990)—or with the Activin A neutralizing antibody MAB3381 was sufficient to sustain proliferation, revealing a prominent role for Activin A in inducing a cytostatic response (Fig 2D). To gain greater insights on the downstream pathway, we boosted Tgf-β receptor activity by combining A83-01 withdrawal with the supplementation of distinct ligands. Activin A was found to enhance the non-canonical arm of Tgf-β signaling—mediated by the Tgf-β activated kinase, Tak1 (encoded by the *Map3k7* gene), and the downstream p38 MAPKs—as well as the accumulation of the cell cycle inhibitor p21 (Fig 2E, Appendix Fig S3A). In contrast, Tgfb1 increased the activity of the canonical Tgf-β pathway—via Smad2/3 phosphorylation, but with little, if any, alteration of p21 levels (Fig 2E, Appendix Fig S3A). This dichotomy prompted us to functionally test the role of the canonical and non-canonical pathway, respectively. Disruption of the canonical pathway, via shRNA-mediated silencing of Smad4, did not alter the cytostatic response upon A83-01 withdrawal (Fig EV4A and B). In contrast, the inhibition of either Tak1 or the structurally related p38α and p38β MAPKs—using a variety of inhibitors (Fig 2F and G, Appendix Fig S3B–D)—was sufficient to ensure organoid expansion in the absence of Tgf-β receptor blockade.

TGF-β receptors, and cytokine-stimulated receptors (e.g., IL-1, TNF, type-I interferons), are known to converge on TAK1-p38 MAPK signaling to activate a variety of downstream factors controlling immune- and stress-related responses, including well-characterized transcriptional programs (Yamaguchi *et al*, 1995; Sato *et al*, 2005; Shim *et al*, 2005; Sorrentino *et al*, 2008). By combining bulk-RNA sequencing and biochemical approaches, we confirmed that in the absence of Tgf-β receptors inhibition, Tak1-p38α/β signaling resulted in phosphorylation and nuclear shuttling of immune-related transcription factors (e.g., Stat1/2, NF-kB), which led to the transcription of immune-related gene sets (e.g., induced by TNF or type-I interferons) (Platanias, 2005), as well as to the phosphorylation of the stress-related kinase Mapkapk2 (Fig 2H and I, Appendix Fig S3E–I). Importantly, Tak1-p38 MAPK activity was associated with the nuclear accumulation of the key cell cycle inhibitors p21 and p16 (Fig 2J, Appendix Fig S3H and I).

Collectively, our data demonstrated that intra-epithelial non-canonical Activin A signaling induce a cytostatic response in mouse prostate organoids.

Evasion from the Tgf-β induced cytostatic response via downregulation of intra-epithelial Activin A signaling

We reasoned that our biobank may offer the opportunity to discover mechanisms of evasion from the Tgf-β induced cytostatic response, mediated by intra-epithelial Activin A signaling, in an unbiased manner. Therefore, we attempted to culture multiple prostate organoid lines in the absence of A83-01, waiting for the potential emergence of clones capable to thrive in these conditions. Out of nine prostate organoid lines (from three distinct mice), six were irreversibly lost within few weeks. Still, three lines survived for an extended period, with two of them eventually adapting to the absence of A83-01 and recovering the ability to be passaged at clonal density (Fig 3A and B, Appendix Fig S4A and B). We performed bulk-RNA sequencing on the C57#1 DLP organoid line in the presence of A83-01, one day after inhibitor withdrawal, and upon adaptation; additionally, we sequenced the C57#3 DLP organoid line in control conditions and following adaptation (Fig 3C). We focused on transcriptional alterations shared by both lines displaying adaptation to A83-01 withdrawal. First, we noticed that gene signatures associated with ATR signaling were strongly upregulated upon adaptation

Figure 2. Intra-epithelial non-canonical Activin A signaling mediates the Tgf-β-induced cytostatic response in mouse prostate organoids.

A Cell cycle analysis by flow cytometry (EdU vs. TO-PRO-3) in complete medium (ENRAD) or in the absence of A83-01 (24 h).

B Detection of proteins secreted by mouse prostate organoids in culture based on click-chemistry enrichment and mass spectrometry analysis (n = 4 biological replicates; data points are shown with crossing line representing mean value).

C IF analysis for selected markers in mouse prostate tissue and organoid sections (scale bar = 50 μm).

D Representative stereoscopic images of mouse prostate organoids cultured in the absence of A83-01, with or without Follistatin (Fst, 500 ng/ml, 6 days), or with or without the Activin A neutralizing antibody MAB3381 (1 μg/ml, 6 days). Scale bar = 1 mm.

E Western blot (WB) analysis in mouse prostate organoids for selected canonical and non-canonical Tgf-β signaling mediators, and the cell cycle inhibitor p21 (Activin A, 50 ng/ml; Tgfb1, 500 ng/ml; 24 h).

F Schematic view of the non-canonical Activin A pathway, including inhibitors used for the experiments described in this figure.

G Representative stereoscopic images of mouse prostate organoids following treatment with Takinib (Tak1 inhibitor; 5 μM, 6 days), SB203580 (p38α/β inhibitor; 10 μM, 6 days) or the structurally unrelated Ralimetinib (p38α/β inhibitor; 1 μM, 7 days). Scale bar = 1 mm.

H Nuclear/Cytoplasmic fractionation and Western blot analysis in mouse prostate organoids for selected signaling mediators in the presence or absence of SB203580 (p38α/β inhibitor; 10 μM, 24 h).

I Gene set enrichment analysis (GSEA) plots displaying significant enrichment for inflammatory response and tumor necrosis factor (TNF) signaling in mouse prostate organoids cultured without A83-01 (24 h) vs. complete medium (ENRAD).

J Nuclear/Cytoplasmic fractionation and western blot analysis in mouse prostate organoids for selected cell cycle regulators, in the presence or absence of SB203580 (p38α/β inhibitor; 10 μM, 24 or 48 h).

Data information: In (A) quantification of cells in S-phase for n = 3 biological replicates are presented in Appendix Fig S2A.
Source data are available online for this figure.

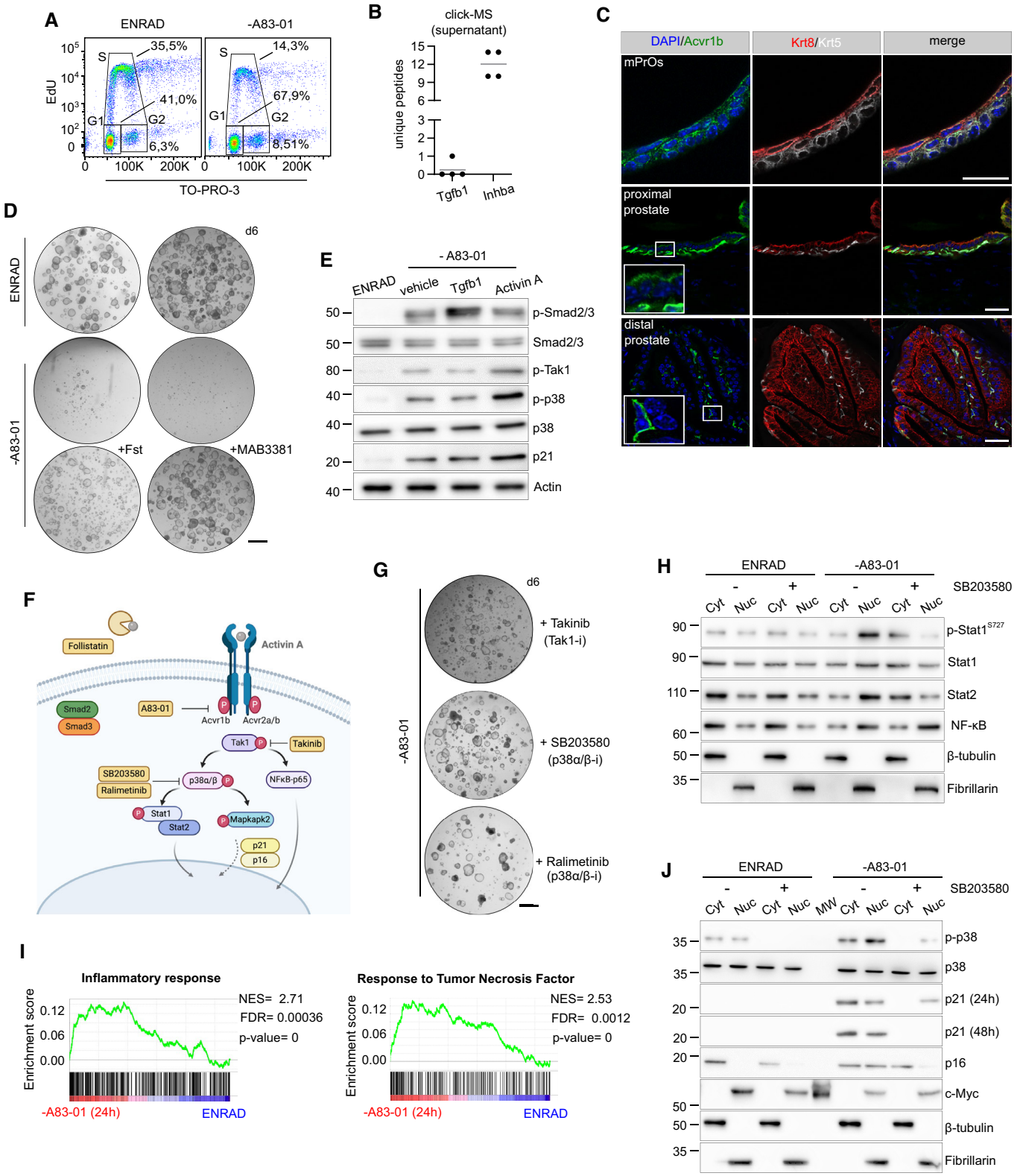

Figure 2.

(Fig 3D), indicating potential DNA replication stress in S-phase, a finding consistent with phosphorylation of the cell cycle Checkpoint kinase 1 (Chek1; Fig 3E). Of note, in the adapted C57#1 DLP line, we detected widespread genomic instability (Figs 3F and EV5A–C) and telomere doublets (Fig 3G and H), a hallmark of DNA replication stress, while retaining an intact p53 pathway (Fig EV5D–F).

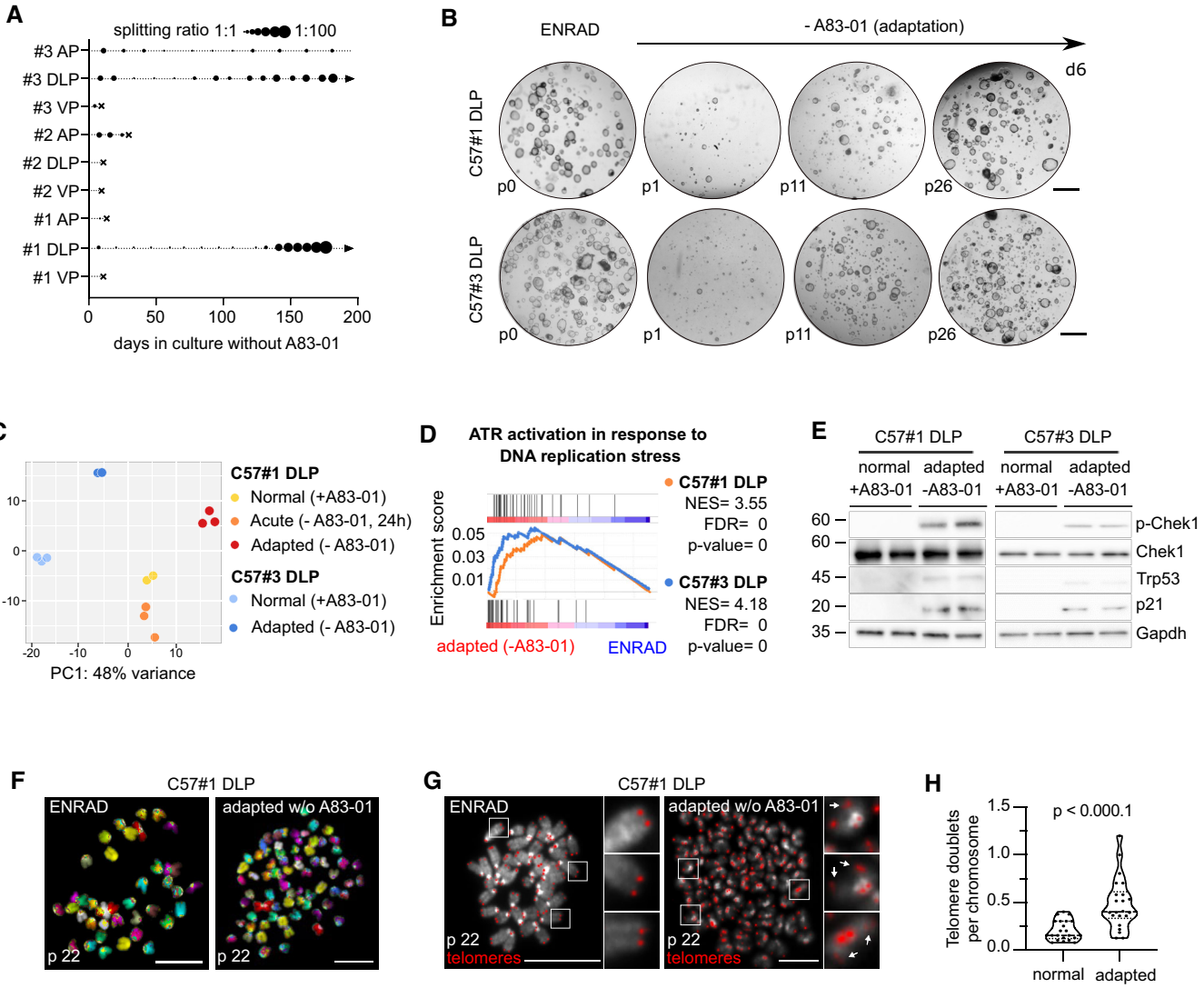

Figure 3. Evasion from the Tgf-β induced cytostatic response leads to DNA replication stress and genomic instability.

A Diagram depicting the expansion of mouse prostate organoid cultures in the absence of the Tgf-β ligand inhibitor A83-01 (n = 3 biological replicates per lobe-specific organoid culture; arrow = continuous expansion; dot = passage; cross = culture loss).

B Representative stereoscopic images of C57BL/6J DLP #1 and #3 mouse prostate organoid lines during adaptation in the absence of A83-01. Scale bar = 1 mm.

C Principal component analysis (PCA) based on bulk RNA-sequencing of C57#1 DLP and C57#3 DLP mouse prostate organoids cultured in normal conditions (ENRAD; n = 3 biological replicates, C57#1 DLP; n = 3 biological replicates, C57#3 DLP), upon acute A83-01 depletion (-A83-01, 24 h; n = 3 biological replicates, C57#1 DLP only) or adaptation (-A83-01, long-term; n = 3 biological replicates, C57#1 DLP; n = 3 biological replicates, C57#3 DLP).

D Gene set enrichment analysis (GSEA) plot displaying significant enrichment for activation of ATR signaling in mouse prostate organoid lines (C57#1 DLP, top; C57#3 DLP, bottom) adapted to grow in the absence of A83-01 vs. normal control organoids cultured in complete medium (ENRAD).

E Western blot analysis in C57#1 and C57#3 DLP mouse prostate organoid lines adapted to grow in the absence of A83-01 vs. normal control organoids cultured in complete medium (ENRAD). Immunoblots are displayed for Chek1 (ATR signaling mediator), Trp53 and p21.

F Representative spectral karyotype (SKY) images of metaphase spreads obtained from C57#1 DLP mouse prostate organoids cultured in normal conditions (ENRAD) or upon adaptation without A83-01. Widespread genomic instability is observed following adaptation. Scale bars = 5 μm.

G, H Representative telomere FISH images—and quantification (n = 2 biological replicates, 20 metaphases per condition)—in C57#1 DLP mouse prostate organoids cultured in normal conditions (ENRAD) or upon adaptation without A83-01. Widespread telomeric instability is observed following adaptation (arrows indicate telomere doublets, one-way ANOVA, scale bars = 10 μm).

Data information: F, quantification of spectral karyotype (SKY) for 25 metaphases per condition in n = 2 biological replicates are presented in Fig EV5B.
Source data are available online for this figure.

Second, in both adapted organoid lines, we observed the downregulation of immune-related transcriptional programs (e.g., type-I interferon-stimulated genes), suggesting an impairment of non-canonical Activin A signaling (Appendix Fig S5A and B). Consistently, we found that adapted organoid lines significantly reduced Activin A secretion in culture (Fig 4A) and that exogenous Activin

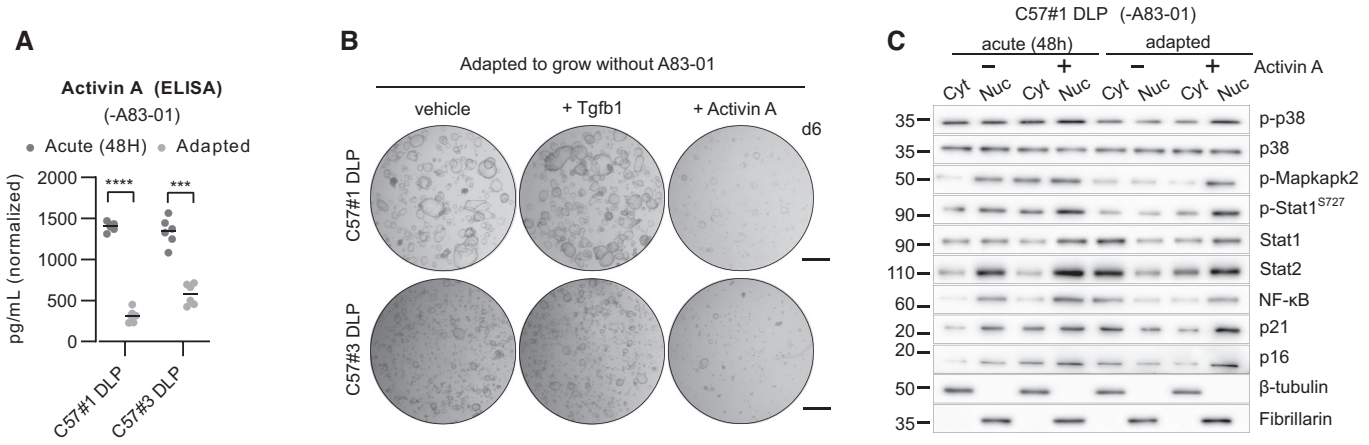

Figure 4. Adaptation occurs via reduction of intra-epithelial Activin A signalling.

A Enzyme-linked immunosorbent assay (ELISA) for Activin A expression in the supernatant of C57#1 and C57#3 DLP mouse prostate organoid lines, upon acute A83-01 removal (48 h) or long-term adaptation (n = 6 biological replicates). Two-way ANOVA, Sidak's test, P-value *** (< 0.001), **** (< 0.0001).

B Representative stereoscopic images of C57#1 and C57#3 DLP mouse prostate organoid lines adapted to the absence of A83-01 and subsequently treated with either Tgfb1 (500 ng/ml, 6 days) or Activin A (50 ng/ml, 6 days). Scale bar = 1 mm.

C Western blot analysis in the C57#1 DLP mouse prostate organoid line upon acute removal (24 h) or long-term adaptation to A83-01 removal, in the presence or absence of Activin A (50 ng/ml, 24 h).

Source data are available online for this figure.

A (but not Tgfb1) was sufficient to restore the cytostatic response (Fig 4B and C, Appendix Fig S6A–C).

Thus, mouse prostate organoids are capable to dampen the Tgf-β-induced cytostatic response by downregulation of intra-epithelial Activin A signaling.

Mouse prostate organoids with reduced intra-epithelial Activin A signaling display enhanced engraftment upon syngeneic transplantation

We wondered whether a reduced intra-epithelial Activin A signaling may release the progenitor proliferative potential in response to basal growth stimuli, within the relative quiescent microenvironment of the adult prostate epithelium. To test this hypothesis, we orthotopically transplanted dissociated mouse prostate organoid cells into immunocompetent syngeneic mice (Fig 5A). Donor cells were injected into the extensive branchial structures of the distal anterior prostate, to avoid damage to the delicate proximal ducts and maximize the probability of retention. Implantation of donor cells into an immunocompetent host tissue characterized by a slow turnover can be considered challenging. Still, we found that, in comparison to control organoid cells, organoid cells adapted to grow without A83-01 implanted with high frequency (Fig 5B) and gave rise to dysplastic foci, characterized by elevated mitotic index, cuboidal histology, and nuclear atypia (Fig 5C and D, Appendix Fig S7).

We conclude that intra-epithelial non-canonical Activin A signaling safeguards quiescence in prostate progenitors.

Discussion

Signaling pathways ensure coordination of tissue development, homeostasis, regeneration, and their disruption can lead to disease. The molecular bases of specific signals are difficult to investigate, due to the challenges of disentangling cellular cross talks *in vivo*, and of establishing representative models *in vitro*. More recently, organoid models in defined media conditions have opened new opportunities for the study of epithelia (Kretzschmar & Clevers, 2016). Benchmarking of these models with their corresponding *in vivo* counterpart is paramount for the correct experimental interpretations (Huch *et al*, 2017). Here, we demonstrated that mouse prostate organoid cultures enable the continuous expansion of epithelial progenitors *in vitro*, including basal, LumP, and PrU cells. Such cell types are predominantly found near the urethra *in vivo*, but also in the distal prostate compartment at low frequency. Our work revealed that progenitor proliferation is dynamically regulated by the antagonistic equilibrium between Egf and non-canonical Activin A signaling, respectively—with at least partial reduction of the latter required for cell cycle progression. The rationale perturbation of additional biochemical signals, and mechanical cues, may enhance progenitor differentiation toward distal luminal cells in culture.

It has long been known that the broad family of TGF-β signals induces a cytostatic response in a large variety of epithelial cells. R-SMADs activation inhibits proliferation of normal cells through the context-dependent transcriptional induction of the potent cell cycle inhibitors $p21^{CIP1}$, $p15^{INK4b}$, $p57^{Kip2}$, and down-regulation of c-Myc. TGF-β/SMAD barrier is frequently defective in colorectal, gastric, ovarian, pancreatic, and head and neck carcinomas depending by somatic mutations or epigenetic silencing of genes encoding core elements of the pathway. In other types of solid malignancies such as breast and prostate cancers, tumor cells become refractory to the antiproliferative action of TGF-β without obvious alterations of principal components of the canonical signaling. Noteworthy, TGF-β pathway expands beyond RSMADs transcriptional program with ligands such as activins and BMPs that increase the complexity of the pathway by playing receptor-, context-, and cell type-dependent

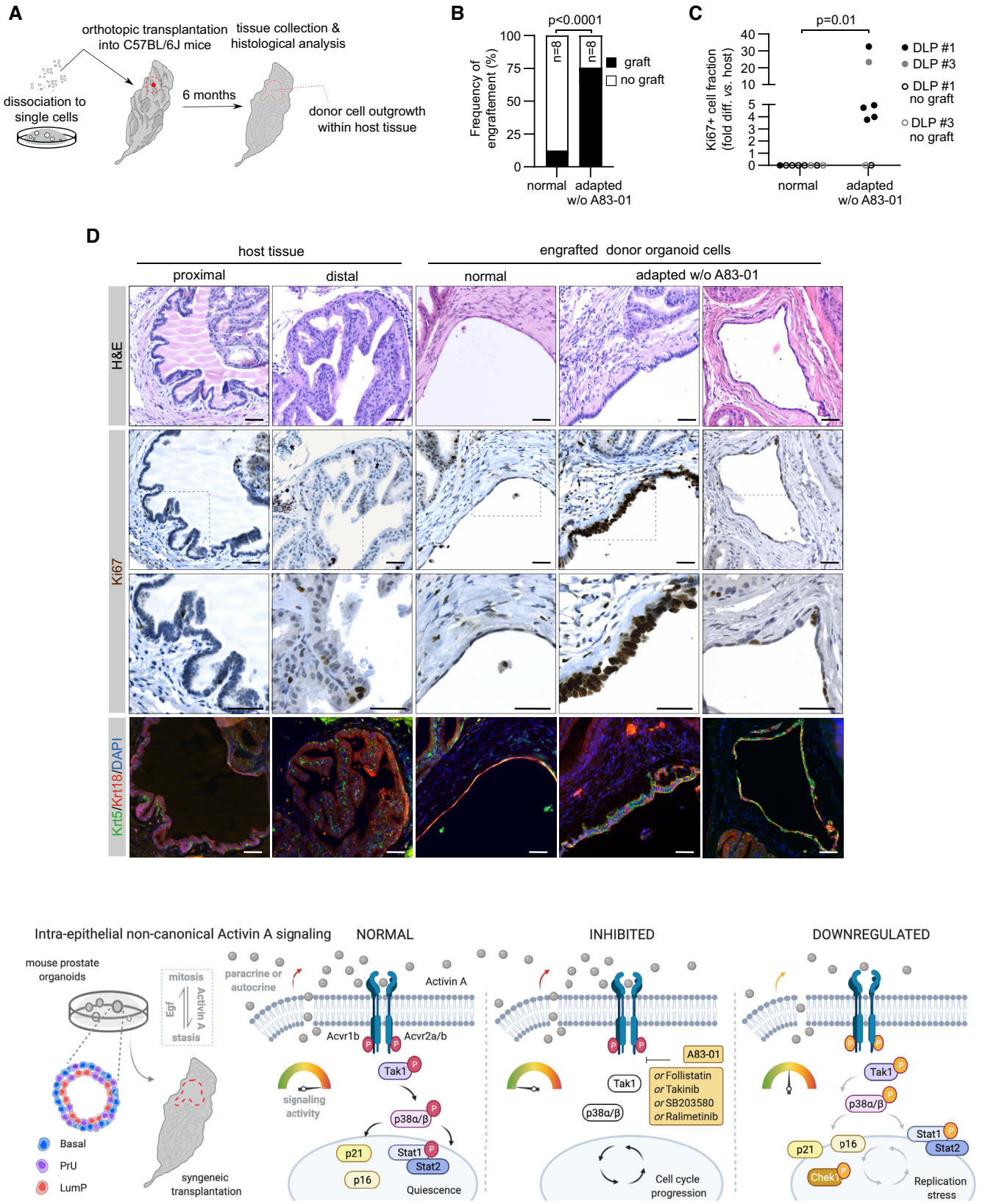

Figure 5.

Figure 5. Enhanced engraftment of mouse prostate organoids with reduced Activin A signalling into immunocompetent hosts.

A Schematic view of the orthotopic transplantation strategy into the anterior prostate lobe of immunocompetent syngeneic C57BL/6J mice.

B Frequency of engraftment (%) of mouse prostate organoid lines (C57#1 DLP and C57#3 DLP) expanded in complete medium (normal C57#1 $n = 8$ mice, normal C57#3 $n = 2$ mice) or adapted to the absence of A83-01 (adapted C57#1 $n = 8$ mice, adapted C57#3 $n = 2$ mice; Binomial test, two-tailed).

C Normalized mitotic ($Ki67^+$) cell index in grafts of mouse prostate organoid lines (C57#1 DLP and C57#3 DLP) expanded incomplete medium conditions (normal) or adapted to the absence of A83-01 (non-parametric Mann–Whitney test).

D Representative H&E, IF, and immunohistochemistry (IHC) analyses of host prostate tissue and engrafted donor organoid cells. Scale bar = 50 μm.

E Model of the molecular pathway primed by Activin A to safeguard quiescence in adult prostate progenitors.

roles in tumorigenesis (Rodgarkia-Dara *et al*, 2006; Sneddon *et al*, 2006; Gao *et al*, 2012; Tarragona *et al*, 2012). Defining the molecular architecture of TGF-β signaling given the specific cellular context will contribute to better understand the pleiotropic effect of the TGF-β pathway in normal and cancer cells and, in turn, to optimize targeting strategies for clinical testing.

TGF-b pathway acting in the prostate has remained poorly understood. Earlier studies pointed to the importance of the Tgf-β family ligand Activin (Cancilla *et al*, 2001; Gold & Risbridger, 2012). At the mechanistic level, DePinho and colleagues initially focused on the role of Smad4 as a proliferative barrier in a *Pten*-loss driven mouse model of prostate cancer (Ding *et al*, 2011). Follow-up studies from the same group and others, carried out in humans and mice, have led to a more complex view (Gerke *et al*, 2015; Lu *et al*, 2017), with the involvement of both canonical and non-canonical pathways.

We propose a prominent role for non-canonical Activin A signaling in safeguarding quiescence in prostate epithelial progenitors (Fig 5E). Our model may be relevant beyond tissue homeostasis and the response to inflammation. Genes encoding for core components of the non-canonical Activin A signaling pathway (e.g., *ACVR2A, MAP3K7*) are frequently lost in prostate cancer, based on large cohorts of patients in the United States (Cancer Genome Atlas Research Network, 2015) and in China (Li *et al*, 2020). Moreover, *MAP3K7* loss has been linked to genomic instability in human prostate cancer cell lines (Washino *et al*, 2019) and found to promote an aggressive transcriptional program in prostate tumors, based on a recent systematic pan-cancer analysis (Paull *et al*, 2021). In contrast, genetic alterations rarely affect TGFB1 receptors (e.g., *TGFBR2*) or SMAD factors (e.g., *SMAD4*), and enhanced canonical TGF-β signaling has been reported in metastatic biopsies in therapy-resistant prostate cancer patients (He *et al*, 2021). We speculate that reduction of non-canonical TGF-β signaling in quiescent progenitor cells might allow cell cycle progression while maintaining residual amounts of p21 and p16 cell cycle inhibitors into the nucleus. This condition likely affects progression and stability of the replication forks during the S phase thus favoring DNA damages and genomic instability in proliferating prostate progenitor cells, sparing the well-known transforming potential of the TGF-β canonical pathway.

Tak1/p38-MAPK signaling stimulated two main sets of effector proteins in prostate progenitors. On the one hand, we observed the nuclear translocation of key negative cell cycle regulators (e.g., p16 and p21). On the other hand, using biochemical and transcriptional analyses, we demonstrated the activation of a broad transcriptional response, reminiscent of those induced by inflammatory cytokines and pathogens. These findings are in line with recent observations on the immune function of structural cells (Krausgruber *et al*, 2020) and suggest a cross talk between the epithelial and immune compartments, beyond the well-known mechanisms of anti-microbial defense. Prostate progenitors—and, perhaps, other types of epithelia cells—may have the ability to signal changes in their proliferative status and, immune cells may have the capability to adjust their function in response.

To test the relevance of intra-epithelial non-canonical Activin A signaling for the enforcement of quiescence in prostate progenitors, we performed experiments *in vitro* and *in vivo*. Our long-term organoid cultures—in the absence of Tgf-β receptor blockade—revealed that cells capable to re-enter cell cycle had downregulated Activin A secretion. Moreover, those cells were also capable to implant and proliferate at increased frequency *in vivo*. While stromal sources of Tgf-β ligands have been previously described in the prostate (Salm *et al*, 2005; Wei *et al*, 2019), our study is the first to demonstrate a key role for intra-epithelial signaling.

Notably, by enabling cell cycle progression in quiescent progenitors while maintaining residual amounts of p21 and p16 cell cycle inhibitors into the nucleus, dysregulation of non-canonical Activin A signaling likely affects the progression and stability of the replication forks during the S phase, which promotes DNA replication stress and genomic instability in proliferating prostate progenitors, a finding that may be relevant to prostate tumor initiation. Indeed, distal LumP cells have been shown to serve as cell-of-origin for prostate cancer (Guo *et al*, 2020). In this regard, our orthotopic transplantation approach may be particularly relevant for investigating the tumorigenic potential of distal progenitor cells.

Finally, P38 MAPK inhibitors—including Ralimetinib—are currently being tested in phase 1/2 clinical trials (Vergote *et al*, 2020). Quiescent tumor progenitors—induced by the broad family of TGF-β signals—are emerging as key mediators of chemotherapy resistance in solid malignancy (Oshimori *et al*, 2015). In advanced prostate cancers with a genetically intact Activin A non-canonical pathway, P38 MAPK inhibitors may force tumors progenitors out of quiescence, improving the efficacy of standard chemotherapy regimens (Quinn *et al*, 2017). While the complexity and pleiotropy of TGF-β signaling has historically complicated drug development (Akhurst & Hata, 2012), the elucidation of cell- and context-specific pathways may lead to novel therapeutic opportunities.

Materials and Methods

Materials availability

All unique/stable reagents generated in this study are available from the Lead Contact upon reasonable request or with a completed Material Transfer Agreement.

Mouse housing and husbandry

All housing systems were following FELASA guidelines and recommendations, concerning animal welfare, health monitoring and

veterinary care, and were in compliance with the Directive 2010/63/UE and its Italian transposition D. L.vo 26/2014. Particular attention was given to prevent animal suffering, by daily check of animals. The CIBIO animal facility is fully accredited and has seven FTE (veterinarians, technicians, and technologists) charged with the care of research animals, including mice. Mice were monitored daily for general health and well-being and sentinel mice are used for quarterly monitoring for specific pathogens.

Wild-type C57BL/6J (JAX # 000664) mice were purchased from the Jackson Laboratory. Wild-type BALB/c (CRL # 028) and CD-1 (CRL # 022) mice were purchased from the Charles River Laboratories. Mice were housed in groups of maximum five animals in IVC cages with food and water ad libitum. Nesting materials and cardboard tunnels were provided as enrichment. The mice were housed in room with 21°C temperature with 12 h light/dark cycle with light gradually rising at 7:00 a.m. and gradually decreasing at 7.00 p.m.

All animal experiments were performed according to the European Communities Council Directive (2010/63/EU) and approved by the Italian Ministry of Health and the University of Trento Animal Welfare Committee (642/2017-PR).

Generation of mouse prostate organoid lines

Mouse prostate organoids were generated from prostate glands collected from adult (6-month- to 1-year-old) C57BL/6J, BALB/c, and CD-1 wild-type males.

Isolation of mouse prostate tissue

Mice were euthanized through CO_2 inhalation and cervical dislocation for confirmation. The anterior (AP), dorso-lateral (DLP), and ventral prostate (VP) lobes were dissected individually, using a transverse cut at the intersection of each lobe with the urethra. Paired lobes were collected for organoid cultures, histology, and immunostaining studies.

Dissociation of mouse prostate tissue to single cells

Prostate tissue was minced into small pieces, washed, resuspended into a digestion buffer—including Collagenase II (1 mg/ml; Life Tech, 17101015) and Dispase II (10 mg/ml; Life Tech 17105041), and transferred into a gentleMACS C tube (Miltenyi Biotec). Tissue fragments were processed by alternating mechanical disruption—using the gentleMACS Dissociator (A.01 -C tube program)—and enzymatic digestion—incubating the solution at 37°C on a tube rotator for 15 min. After three cycles, the cell suspension was pelleted, resuspended in TrypLE (Life Tech, 12605010), and incubated for 5 min at 37°C. After two washes, the cell suspension was filtered through a 70-μm strainer and counted.

3D prostate organoid cultures

Dissociated prostate cells were resuspended in 80% growth factor-reduced basement matrix (either Matrigel®, Corning, 356231; or BME-2®, AMSBIO, 3533) and seeded at the concentration of approximately 50,000 cells/ml, by depositing at least six 40 μl drops at the bottom of a non-tissue culture-treated plate. Basement matrix domes were left to solidify for 15 min and covered with ENRAD medium—including Egf (50 ng/ml; PeproTech, 315-09), Noggin (100 ng/ml; PeproTech, 120-10C), R-Spondin1 (10% conditioned medium), A83-01 (200 nM; Tocris, 2393), and dihydrotestosterone (10 nM; Merck, 10300)—supplemented with Y-27632 (10 μM; Calbiochem, 146986-50-7) and ATRA (10 mM; Merck R2625). Organoids were cultured in a standard tissue culture incubator, with medium replacement every 2–3 days. After 6 days from the initial seeding, organoids were imaged with a Leica MZ16F stereomicroscope and organoid forming efficiency was calculated. For subsequent passages, the basement membrane was dissolved using a recovery solution—including Dispase II (1 mg/ml)—and organoids were dissociated to small clumps/single cells as described above, using TrypLE. Following the first passage, organoids were seeded at the concentration of approximately 25,000 cells/ml. Growth factors and small molecules used in this study are described in Appendix Table S1.

Lentiviral transduction of organoids

Organoids were dissociated to single cells, and approximately 50,000 cells were transduced for each condition. Spinoculation was performed in a low-adhesion 96-well plate using 0.6 RTU of lentiviral solution, supplemented with polybrene (4 μg/ml; Sigma-Aldrich, H9268) and complete medium (ENRAD) to reach a final reaction volume of 300 μl. The plate was sealed with parafilm and centrifuged for 1 h at 600 *g*. Afterwards, the cells were resuspended in 200 μl of complete medium (ENRAD), supplemented with Y-27632 (10 μM), and incubated in suspension at 37°C for 4–6 h. After centrifugation, the cell pellet was resuspended in 80% basement matrix and seeded as described above. Antibiotic selection was initiated two days post-transduction. The following plasmids were used: pLenti-AIB-EGFP (kindly donated by Massimo Pizzato), pSUPER-retro-puro-Smad4 (Addgene #89829), and pSUPER-retro-puro-GFP shRNA (Addgene #30519), MISSION® shRNA Lentiviral Transduction Particles (AcvrIb, Merck SHCLNV-TRCN0000022578, SHCLNV-TRCN0000345027).

Orthotopic transplantation of organoid in syngeneic recipient mice

Orthotopic transplantation of organoids was performed into the prostate of month-old syngeneic immune-competent C57BL/6J 6 adult mice that were randomly assigned to the control or experimental arm. Organoids were dissociated as described above, with 50,000 cells per injection resuspended in 10 μl of 50% basement matrix, supplemented with methylene blue (as tracer). Upon abdominal incision of the host, the left anterior prostate lobe was exposed and injected into the distal part. Injection was performed blinded to randomization. Mice were regularly monitored and sacrificed after 6 months for tissue collection and histopathological analysis.

Flow cytometry

Organoids were dissociated to single cells as described above. For cell surface antigen expression analysis, cells were incubated with anti-Cd24a-APC and Sca-1-PE-Cy7 antibodies (1:800 dilution) at 4°C for 20–30 min, followed by one wash with FACS buffer (1% FBS, 1mM EDTA). Cells were resuspended in FACS buffer, supplemented with 1 μM propidium iodide (Life Tech, P3566) for dead cell

exclusion, before proceeding to the analysis. For DNA content analysis, cells were resuspended in 100 µl ice-cold PBS and transferred to a 15-ml tube. About 900 µl of ice-cold EtOH 70% were added dropwise while agitating the cell suspension on a vortex. Cells were then fixed for at least 2 h at −20°C before proceeding with three washing steps in PBS, alternated by centrifugation (700 *g*, 5 min) with no brake. Afterwards, cell pellet was resuspended in 100 µl of DNAse-free RNAseA (0.5 µg/ml; Life Tech, 12091021) and incubated for 10 min at 37°C. Cells were incubated with 100 µl of propidium iodide (50 µg/ml) for 30 min, at room temperature, before proceeding to the analysis. For cell cycle analysis, organoids were treated with 10 µM EdU for 3 h. Then, organoids were harvested, dissociated into single cells, and filtered through a 30-µm strainer. Cells were pelleted and stained with the Click-iT™ Plus EdU Alexa Fluor™ 488 Flow Cytometry Assay Kit (Thermo Fisher Scientific, C10632), according to the manufacturer protocol. After the incorporation of the fluorescent probe, cells were incubated with TO-PRO™-3 Iodide (Life Tech, T3695) to stain for DNA content, before proceeding to the analysis. Flow cytometry was performed with a FACS Canto (BD) analyser, and data were analyzed with Flow Jo v.10.

Histology, immunostaining, and live imaging

Organoids were cultured for 5–7 days, released from the basement membrane as described above, seeded in a neutralized collagen type-I solution (Corning, 354249), and cultured for additional 24 h, before proceeding to fixation in 4% paraformaldehyde (Sigma-Aldrich, P6148) for 5 h, at room temperature. Prostate tissue was harvested and immediately fixed using the same conditions. Paraffin embedding and 5 µm sectioning were carried out according to standard procedures. For immunofluorescence studies, antigen retrieval was performed using a citrate-based buffer (pH 6.0; Vector Lab, H3300). Slides were incubated in blocking solution (5% FBS + 0.1% Triton-X in PBS), before proceeding to staining with primary antibodies, at 4°C, overnight. After three washes, spectrally distinct fluorochrome-conjugated antibodies were incubated for 2 h at room temperature. After three additional washes, samples were counterstained with Hoechst 33342 (Abcam, ab145597), and the coverslip was applied, using Fluor-Save mounting medium (Merck, 345789). For immunohistochemistry studies, a similar protocol was followed, but using biotin-conjugated secondary antibodies. The detection was performed using the Vectastain® Elite ABC Peroxidase kit (Vector Labs, PK-6100) according to the manufacturer instructions. The final reaction was blocked by washing slides with water, and coverslips were applied using the DPX mounting medium (Sigma, 06522). For hematoxylin and eosin (H&E) staining, deparaffinized sections were incubated with Gill hematoxylin (Merck, GH5232) for 2 min and washed with water. Samples were washed with ethanol, incubated with eosin Y (Merck, HT110132) for 3 min, washed again twice with ethanol, and treated with xylene, before mounting the coverslips in phenol-based mounting medium. For immunostaining with anti-Egfr and anti-Acvr1b antibodies, the urogenital apparatus was isolated, snap-frozen in 2-methyl-buthanol cooled in liquid nitrogen, and cryo-sectioned at 20 µm. Tissue slides were fixed in 4% paraformaldehyde for 20 min at room temperature, before proceeding as described above. For live imaging, organoids were stably transduced with pLenti-AIB-EGFP. Images were acquired using either a Zeiss Axio Imager M2, or a Zeiss Axio Observer Z1 Apotome, or a Leica TCS SP8 Confocal. Image analysis was performed with the Zeiss ZEN software or ImageJ (v.2.0.0-rc-69/1.52i) (Rueden *et al*, 2017). Primary antibodies are listed in the Appendix Table S2.

RNA extraction

Total RNA was extracted using the RNeasy Plus Micro kit (Qiagen, 74034) according to the manufacturer instructions and analyzed with an Agilent BioAnalyzer 2100 to confirm integrity (RIN > 8), before proceeding with downstream applications.

End-point semi-quantitative and quantitative real-time PCR

RNA was retrotranscribed into cDNA using the iScript™ cDNA synthesis kit (BioRad, 1708891). End-point PCR was performed using Phusion Universal qPCR Kit (Life Tech, F566L), with PCR products visualized by standard gel electrophoresis. For quantitative real-time gene expression analysis, the qPCRBIO SyGreen Mix (PCRBiosystems, PB20.14-05) was used according to the manufacturer instructions. At least three biological replicates were run for each sample, using the CFX96 Real-Time PCR thermocycler (Bio-Rad). The data were processed using Bio-Rad CFX Manager software (v.3.1), while gene expression quantification and statistical analyses were performed with GraphPad PRISM (v.6.01). Primer sequences are included in the Appendix Table S3.

RNA sequencing and data analysis

cDNA libraries were prepared with TruSeq stranded mRNA library prep Kit (Illumina, RS-122-2101) using 1 µg of total RNA. RNA sequencing was performed on an Illumina HiSeq 2500 Sequencer using standard Rapid Run conditions at the Next-Generation Sequence Facility of University of Trento. The obtained reads were 100 bp long, single ends, and 25 million on average for each sample. FASTQ file from Illumina HiSeq2500 sequencing machine underwent adapter removal and quality-base trimming using Trimmomatic-v0.35. Genomic alignments were performed onto the Mouse genome (mm10 assembly version) using STAR-v2.6.0 aligner with a maximum mismatch of two and default settings for all other parameters. Then, uniquely mapped reads were selected and processed with HTSeq-count v0.5.4 tool to obtain gene-level raw counts based on GRCm38.92 Ensembl (www.ensembl.org) annotation. Genes with CPM (Counts Per Million) < 1 in all replicates were considered unexpressed and hence removed from the analysis. TMM (Trimmed Mean of *M* values) normalization and CPM conversion were next performed to obtain gene expression levels for downstream analyses. For each comparison, differential expression testing was performed using the edgeR-3.20.9 statistical package. According to the edgeR workflow, both common (all genes in all samples) and separate (gene-wise) dispersions were estimated and integrated into a Negative Binomial generalized linear model to moderate gene variability across samples. For each comparison, genes having a log Fold-change outside the range of ± 1.5 and an FDR q-value equal or smaller than 0.01 were considered as differentially expressed between the two groups. Deposited RNA sequencing datasets are described in Appendix Table S4.

Gene set enrichment analysis

For the gene set enrichment analysis, the GSEA software (v4.0.3) was run in the 'pre-ranked' mode using the Fold-change as a ranking metric and an FDR enrichment threshold of 0.25. Gene sets were directly obtained from the Molecular Signature (MSig) database (http://software.broadinstitute.org/gsea/msigdb) focusing on all available sets reported in the following MSigDB collections: C2 (curated gene sets): Biocarta, Kegg, Reactome; C5 (Gene ontology): Biological Processes, Cellular Component, Molecular Function; C6 (oncogenic signatures) and C7 (immunologic signatures).

Principal component analysis

Principal component analysis (PCA) was performed using the DESeq2 R-package (Love *et al*, 2014) as follows: normalized counts (CPM) were firstly converted into a DESeqDataset object through a DESeqDatasetFromMatrix function with default parameters and transformed through the variantStabilizingTransformation function to stabilize variance-mean relation across samples. Then, transformed data were analyzed by PCA (plotPCA function) generating a two-dimensional space where the two first components are represented.

Single cell expression analysis

Log-2 transformed count data were downloaded from the Broad Institute Single Cell Portal (https://singlecell.broadinstitute.org/single_cell/study/SCP1080/anterior). The clusters' annotations for each cell were retrieved as assigned by Crowley *et al* (2020) and employed for the violin plots generation.

Subcellular fractionation and western blotting

Cell pellets from organoid cultures were obtained as previously described and lysed in fresh RIPA buffer (50 mM Tris–HCl, pH 7.5, 150 mM NaCl, 1% Triton X-100, 1% sodium deoxycholate, 1% NP-40) supplemented with protease (Halt™ protease inhibitor cocktail, Life Tech, 87786) and phosphatase inhibitors (Phosphatase-Inhibitor Mix II solution, Serva, 3905501). Nuclear/cytoplasmic fractionation was performed using NE-PER Nuclear and Cytoplasmic Extraction Kit (Life Tech, 78833) according to the manufacturer instructions. Protein concentrations were measured using the BCA Protein Assay Kit (Pierce™ BCA Protein Assay kit, Thermo Fisher Scientific, 23225) and a Tecan Infinite M200 Plate Reader.

Protein extracts were resolved via SDS–PAGE, transferred to polyvinylidene difluoride (PVDF) membrane (Merck, GE10600023) using a wet electroblotting system (Bio-Rad). The membranes were blocked with 5% non-fat dry milk or 5% BSA in TBS-T (50 mM Tris–HCl, pH 7.5, 150 mM NaCl, 0.1% Tween20) for 1 h, at room temperature, and then incubated with gentle shaking with designated primary antibodies overnight, at 4°C. Membranes were incubated with HRP-conjugated secondary antibody in blocking buffer for 1 h at room temperature. Immunoreactive bands were detected using ECL LiteAblot plus kit A + B (Euroclone, GEHRPN2235) with an Alliance LD2 device and software (UVITEC). Primary antibodies are provided in the Appendix Table S2.

Click-it chemistry-based mass spectrometry analysis

Organoids were seeded at the approximate concentration of 50,000 cells/ml, depositing seven 40 µl domes per individual well of a six-well non-tissue culture plate. Three wells were used for each condition. Following methionine depletion (2 h), organoids were grown overnight at 37°C with L-azidohomoalanine (AHA) medium. Conditioned supernatants were collected, supplemented with protease inhibitors, and stored at −80°C until further processing. CLICK-IT enrichment of AHA-labeled secreted proteins was performed with the Click-iT™ protein enrichment kit (Thermo Fisher Scientific, C10416) as previously described (Eichelbaum *et al*, 2012; Eichelbaum & Krijgsveld, 2014). Following trypsin digestion, peptides were purified by reversed-phase (C18) stage-tip purification (Rappsilber *et al*, 2007). LC-MS/MS analysis was performed by an EASY-LC 1000 coupled to a Q-Exactive mass spectrometer (Thermo Fisher Scientific). LC-MS/MS data analysis was conducted using the MaxQuant/Perseus software suite.

Enzyme-linked immunosorbent assay (ELISA)

Activin A quantification was performed using the corresponding Quantikine ELISA Kit (R&D Systems, DAC00B) according to the manufacturer instructions.

Karyotype analysis

Organoid cultures were treated with nocodazole (15 µM; Sigma, SML1665) for 5 h. Organoids were recovered from basement membrane, and 900 µl/sample of 50 mM KCl were added to the cell pellet dropwise, followed by 10 min of incubation at 37°C. After centrifugation (200 *g*, 5 min) 900 µl/sample of Carnoy's fixative (methanol/acetic acid 3:1) was added dropwise. Samples were resuspended and incubated for 10 min at 37°C, followed by three washes with methanol/acetic acid 2:1. Approximately 25,000 cells/samples were resuspended in 50 µl and dropped from at least 1 meter of height, directly on a glass slide. After air-drying, the glass slide was incubated with Hoechst 33342, at room temperature, for 10 min, and then washed with methanol/acetic acid 2:1 for 5 min. After air-drying, coverslips were mounted with ProLong Gold Antifade (Invitrogen, P36934). Images were acquired at the Zeiss Observer Z1 microscope and analyzed with ImageJ (v2.0.0-rc-69/1.52i).

Multicolor FISH (M-FISH), Chromosome painting and Telomeric FISH

For M-FISH, fixed cells were dropped onto glass slides and hybridized with the 21XMouse Multicolor FISH Probe Kit (MetaSystems, D-0425-060-DI), as previously described (Nieri *et al*, 2013). Briefly, the slides were denatured in 0.07 N NaOH and then rinsed in a graded ethanol series. The probe mix was denatured using a MJ mini personal thermal cycler (Bio-Rad) with the following program: 5 min at 75°C, 30 s at 10°C, and 30 min at 37°C. The probe was added to the slides and the coverslip was sealed using rubber cement. The samples were then hybridized in a humidified chamber at 37°C for 48 h, washed in saline-sodium citrate (SSC) buffer for 5 min at 75°C, and finally counterstained with DAPI (Abcam, 6843.2), in Vectashield mounting medium. Metaphases were

visualized and captured using a Zeiss Axio-Imager M1 microscope. The karyotyping and cytogenetic analysis of each single chromosome was performed using the M-FISH module of the ISIS software (MetaSystems). A total of 25 metaphases for each sample spreads were analyzed in two biological replicates.

For chromosome painting, fixed cells were dropped onto glass slides and hybridized with enumeration XMP painting probes specific for chromosomes X (red label) and chromosome Y (green label; MetaSystems, D-1420-050-OR, D-1421-050-FI) following the manufacturer instructions. Briefly, probes were applied to the slides, denatured at 75°C for 2 min, and then incubated at 37°C overnight. The slides were washed in SSC and counterstained with DAPI in antifade reagent (MetaSystems, D-0902-500-DA). Metaphases were visualized and captured using a Zeiss Axio-Imager M1 microscope. A total of 100 metaphases were analyzed for each sample in two biological replicates.

For telomeric FISH, staining was performed as previously described (Samper *et al*, 2000). Briefly, slides and the Cy3 linked telomeric (TTAGGG)3 PNA probe, (DAKO Cytomatation, K5326) were co-denatured at 80°C for 3 min, and hybridized for 2 h at room temperature, in a humidified chamber. After hybridization, slides were washed and then dehydrated with an ethanol series and air-dried. Finally, slides were counterstained with DAPI and Vectashield. Images were captured at 63× magnification using a Zeiss Axio-Imager M1 microscope, and the telomere signals were analyzed using the ISIS software (MetaSystems). Telomere doublets frequency was calculated as the ratio between the number of doublets signals and the total number of chromosomes in each metaphase analyzed (Berardinelli *et al*, 2019). At least 20 metaphases in two biological replicates were analyzed.

Chemicals and recombinant proteins used in this study are described in Appendix Table S5.

Quantification and statistical analysis

The *in vitro* experiments were not randomized, and the investigators were not blinded to allocation during experiments and outcome assessment. The *in vivo* transplantation experiments were randomized, and the investigators were blinded to allocation during experiments and outcome assessment. The *in vitro* experiments were carried out on organoid lines derived from at least two distinct animals and repeated at least in three biological replicates. The *in vivo* transplantation experiments were based on two distinct organoid lines and were repeated at least two times. No statistical methods were used to predetermine sample size. Data collection was performed using Microsoft Office Excel 2016–2018 and statistical analysis was performed using GraphPad Prism 6 software. The number of replicates, the format of the data, and the statistical tests are indicated in figure legends. P-values < 0.05 were considered significant.

Software and algorithms used in this study are described in Appendix Table S6.

Data availability

The datasets produced in this study are available in the following databases:

RNA sequencing data have been deposited in the BioProject with identifier PRJNA659468 and are available at the following link:

https://www.ncbi.nlm.nih.gov/bioproject/?term = PRJNA659468.

Proteomic data have been deposited in ProteomeXchange with identifier PXD029660 and are available at the following link:

http://proteomecentral.proteomexchange.org/cgi/GetDataset?ID = PXD029660.

Expanded View for this article is available online.

Acknowledgements

We are grateful to Francesca Demichelis, Alberto Inga, Giannino del Sal, Marco Marcia, and Karuna Ganesh, for critical reading of the manuscript, and, Luciano Conti, Alessio Zippo, Luca Fava, Fulvio Chiacchiera, Davide Bressan, Luca Tiberi, Massimo Lopes, Alberto Briganti, Matteo Bellone and Marianna Kruithof-de Julio for fruitful discussions. We thank Francesca Demichelis, Massimo Pizzato, Luca Fava, Yari Ciribilli, and Valeria Poli, for sharing reagents. We thank Veronica de Sanctis, Roberto Bertorelli and Paola Fassan of the Next Generation Sequencing Facility of the University of Trento for RNA sequencing. We also thank Sergio Robbiati and Marta Tarter of the CIBIO Model Organism Facility, Marina Cardano of the CIBIO Cell Technology Facility, Giorgina Scarduelli and Michela Roccuzzo of the CIBIO Advanced Imaging Facility, Isabella Pesce of the CIBIO Cell Analysis and Separation Facility, Valentina Adami and Michael Pancher of the CIBIO High-Throughput Screening Facility, and Isabelle Bonomo for assistance with experiments. Illustrations were created with Inkscape and BioRender.com. This study was primarily supported by grants from the Giovanni Armenise-Harvard Foundation (Career Development Award to A.L.), the Lega Italiana Lotta ai Tumori (LILT-Bolzano to A.L.), the Italian Ministry of Education, University and Research (MIUR PRIN 2017 to A.L.), the Associazione Italiana per la Ricerca sul Cancro (AIRC MFAG 2017-ID 20621 to A.R.), the NIH (R01CA238005 to M.M.S.)—and by core funding from the University of Trento. Individual fellowships were awarded from the United States Department of Defence (W81XWH-18-1-0424 to F.C.), the European Union (H2020-MSCA 749795 to A.Be.), the Fondazione Umberto Veronesi (FUV 2016 and 2017 to F.C., FUV 2016 to A.A., and FUV 2018 to A.Be.), and the University of Trento (Ph.D. fellowship to V.F, and D.D.F.). Open Access Funding provided by Universita degli Studi di Trento within the CRUI-CARE Agreement.

Author contributions

Francesco Cambuli: Conceptualization; Data curation; Formal analysis; Supervision; Validation; Investigation; Visualization; Methodology; Writing—original draft; Writing—review and editing. **Veronica Foletto:** Conceptualization; Data curation; Formal analysis; Validation; Visualization; Methodology; Writing—original draft. **Alessandro Alaimo:** Data curation; Formal analysis; Validation; Investigation; Visualization; Methodology; Writing—review and editing. **Dario De Felice:** Data curation; Formal analysis; Validation; Investigation; Visualization; Methodology; Writing—review and editing. **Francesco Gandolfi:** Data curation; Formal analysis; Methodology. **Maria Dilia Palumbieri:** Data curation; Formal analysis; Investigation. **Michela Zaffagni:** Data curation; Formal analysis; Investigation. **Sacha Genovesi:** Data curation; Formal analysis; Investigation; Visualization; Methodology. **Marco Lorenzoni:** Data curation; Formal analysis; Investigation. **Martina Celotti:** Data curation; Formal analysis; Investigation. **Emiliana Bertossio:** Data curation; Formal analysis; Investigation. **Giosuè Mazzero:** Formal analysis; Investigation; Methodology. **Arianna Bertossi:** Data curation; Formal analysis; Investigation; Methodology. **Alessandra Bisio:** Resources; Investigation; Methodology. **Francesco Berardinelli:** Data curation; Formal analysis; Validation; Investigation; Visualization; Methodology. **Antonio Antoccia:** Data curation; Formal

analysis; Validation; Investigation; Visualization; Methodology. **Marco Gaspari:** Data curation; Formal analysis; Investigation; Methodology. **Mattia Barbareschi:** Data curation; Formal analysis; Investigation; Methodology. **Michelangelo Fiorentino:** Data curation; Formal analysis; Investigation; Methodology. **Michael M Shen:** Data curation; Formal analysis; Funding acquisition; Investigation; Methodology; Writing—review and editing. **Massimo Loda:** Data curation; Formal analysis; Methodology; Writing—review and editing. **Alessandro Romanel:** Data curation; Formal analysis; Investigation; Methodology; Writing—review and editing. **Andrea Lunardi:** Conceptualization; Data curation; Formal analysis; Supervision; Funding acquisition; Validation; Investigation; Visualization; Methodology; Writing—original draft; Project administration; Writing—review and editing.

In addition to the CRediT author contributions listed above, the contributions in detail are:

FC made initial observations and designed the project in consultation with AL; FC, VF and AL designed the experiments with the contribution of AAla and DDF regarding the Tak1/p38 MAPK signaling; FC, with the contribution of MZ, generated and characterized the normal prostate organoid lines described in this study; FC, with the contribution of MDP, carried out the wet-lab-based experiments defining the role of non-canonical Tgf-β signaling in the control of epithelial progenitor proliferation and the ability of progenitors to spontaneously evade such regulatory mechanism; FC, VF, EB, and DDF characterized the consequences of non-canonical Tgf-β signaling evasion in organoid cultures; VF generated the sh-Smad4 organoid line, with the contribution of DDF and MC, carried out the pharmacological studies on Tak1/p38 MAPK signaling; VF, AAla, and DDF performed biochemical studies on cell cycle regulators and mediators of the type-I interferon-like response; VF, DDF, SG, GM, and AL performed orthotopic transplantations; ML and MG executed Click-it mass spectrometry experiments and analyzed the data; ABe contributed to flow cytometry; SG executed immunostaining experiments and contributed to image acquisition; ABi contributed to the characterization of p53 function in organoids; FB and AAnt carried out and analyzed chromosome painting and FISH studies; MB, MF and ML provided histopathological annotations; FG and AR performed the computational analyses; MMS contributed to the interpretation of data; FC and VF assembled the figures; FC wrote the first draft of the manuscript; FC, VF, and AL edited the manuscript with inputs from FB, AAnt, AR, ML and MMS; AL acquired the main funding sources AL, AAla, DDF, and SG, revised the manuscript with inputs from FC, VF, and MMS.

Disclosure and competing interests statement

The authors declare that they have no conflict of interest.

References

Akhurst RJ, Hata A (2012) Targeting the TGFβ signalling pathway in disease. *Nat Rev Drug Discov* 11: 790 – 811

Bailey P, Chang DK, Nones K, Johns AL, Patch A-M, Gingras M-C, Miller DK, Christ AN, Bruxner TJC, Quinn MC *et al* (2016) Genomic analyses identify molecular subtypes of pancreatic cancer. *Nature* 531: 47 – 52

Barros-Silva JD, Linn DE, Steiner I, Guo G, Ali A, Pakula H, Ashton G, Peset I, Brown M, Clarke NW *et al* (2018) Single-cell analysis identifies LY6D as a marker linking castration-resistant prostate luminal cells to prostate progenitors and cancer. *Cell Rep* 25: 3504 – 3518.e6

Berardinelli F, Tanori M, Muoio D, Buccarelli M, di Masi A, Leone S, Ricci-Vitiani L, Pallini R, Mancuso M, Antoccia A (2019) G-quadruplex ligand RHPS4 radiosensitizes glioblastoma xenograft in vivo through a differential targeting of bulky differentiated- and stem-cancer cells. *J Exp Clin Cancer Res* 38: 311

de Bono JS, Guo C, Gurel B, De Marzo AM, Sfanos KS, Mani RS, Gil J, Drake CG, Alimonti A (2020) Prostate carcinogenesis: inflammatory storms. *Nat Rev Cancer* 20: 455 – 469

Cancer Genome Atlas Research Network (2015) The molecular taxonomy of primary prostate cancer. *Cell* 163: 1011 – 1025

Cancilla B, Jarred RA, Wang H, Mellor SL, Cunha GR, Risbridger GP (2001) Regulation of prostate branching morphogenesis by activin A and follistatin. *Dev Biol* 237: 145 – 158

Chua CW, Shibata M, Lei M, Toivanen R, Barlow LJ, Bergren S, Badani KK, McKiernan JM, Benson MC, Hibshoosh H *et al* (2014) Single luminal epithelial progenitors can generate prostate organoids in culture. *Nat Cell Biol* 16: 951 – 961, 1–4

Crowell PD, Fox JJ, Hashimoto T, Diaz JA, Navarro HI, Henry GH, Feldmar BA, Lowe MG, Garcia AJ, Wu YE *et al* (2019) Expansion of luminal progenitor cells in the aging mouse and human prostate. *Cell Rep* 28: 1499 – 1510.e6

Crowley L, Cambuli F, Aparicio L, Shibata M, Robinson BD, Xuan S, Li W, Hibshoosh H, Loda M, Rabadan R *et al* (2020) A single-cell atlas of the mouse and human prostate reveals heterogeneity and conservation of epithelial progenitors. *Elife* 9: e59465

Crowley L, Cambuli F, Aparicio L, Shibata M, Robinson BD, Xuan S, Li W, Hibshoosh H, Loda M & Rabadan R et al (2020). Broad Institute Single Cell Portal (https://singlecell.broadinstitute.org/single_cell/study/SCP1080/anterior). [DATASET]

David CJ, Massagué J (2018) Contextual determinants of TGFβ action in development, immunity and cancer. *Nat Rev Mol Cell Biol* 19: 419 – 435

De Marzo AM, Nelson WG, Meeker AK, Coffey DS (1998) Stem cell features of benign and malignant prostate epithelial cells. *J Urol* 160: 2381 – 2392

Derynck R, Budi EH (2019) Specificity, versatility, and control of TGF-β family signaling. *Sci Signal* 12: eaav5183

Ding Z, Wu C-J, Chu GC, Xiao Y, Ho D, Zhang J, Perry SR, Labrot ES, Wu X, Lis R *et al* (2011) SMAD4-dependent barrier constrains prostate cancer growth and metastatic progression. *Nature* 470: 269 – 273

Drost J, Karthaus WR, Gao D, Driehuis E, Sawyers CL, Chen Y, Clevers H (2016) Organoid culture systems for prostate epithelial and cancer tissue. *Nat Protoc* 11: 347 – 358

DuPre NC, Flavin R, Sfanos KS, Unger RH, To S, Gazeeva E, Fiorentino M, De Marzo AM, Rider JR, Mucci LA *et al* (2018) Corpora amylacea in prostatectomy tissue and associations with molecular, histological, and lifestyle factors. *Prostate* 78: 1172 – 1180

Eichelbaum K, Winter M, Berriel Diaz M, Herzig S, Krijgsveld J (2012) Selective enrichment of newly synthesized proteins for quantitative secretome analysis. *Nat Biotechnol* 30: 984 – 990

Eichelbaum K, Krijgsveld J (2014) Combining pulsed SILAC labeling and click-chemistry for quantitative secretome analysis. *Methods Mol Biol* 1174: 101 – 114

Gao H, Chakraborty G, Lee-Lim AP, Mo Q, Decker M, Vonica A, Shen R, Brogi E, Brivanlou AH, Giancotti FG (2012) The BMP inhibitor Coco reactivates breast cancer cells at lung metastatic sites. *Cell* 150: 764 – 779

Gerke TA, Martin NE, Ding Z, Nuttall EJ, Stack EC, Giovannucci E, Lis RT, Stampfer MJ, Kantoff PW, Parmigiani G *et al* (2015) Evaluating a 4-marker signature of aggressive prostate cancer using time-dependent AUC. *Prostate* 75: 1926 – 1933

Gerstung M, Jolly C, Leshchiner I, Dentro SC, Gonzalez S, Rosebrock D, Mitchell TJ, Rubanova Y, Anur P, Yu K *et al* (2020) The evolutionary history of 2,658 cancers. *Nature* 578: 122 – 128

Gold E, Risbridger G (2012) Activins and activin antagonists in the prostate and prostate cancer. *Mol Cell Endocrinol* 359: 107 – 112

Guo W, Li L, He J, Liu Z, Han M, Li F, Xia X, Zhang X, Zhu Y, Wei YU *et al* (2020) Single-cell transcriptomics identifies a distinct luminal progenitor cell type in distal prostate invagination tips. *Nat Genet* 52: 908 – 918

He MX, Cuoco MS, Crowdis J, Bosma-Moody A, Zhang Z, Bi K, Kanodia A, Su M-J, Ku S-Y, Garcia MM *et al* (2021) Transcriptional mediators of treatment resistance in lethal prostate cancer. *Nat Med* 27: 426 – 433

Henry GH, Malewska A, Joseph DB, Malladi VS, Lee J, Torrealba J, Mauck RJ, Gahan JC, Raj GV, Roehrborn CG *et al* (2018) A cellular anatomy of the normal adult human prostate and prostatic urethra. *Cell Rep* 25: 3530 – 3542.e5

Huch M, Knoblich JA, Lutolf MP, Martinez-Arias A (2017) The hope and the hype of organoid research. *Development* 144: 938 – 941

Joseph DB, Henry GH, Malewska A, Iqbal NS, Ruetten HM, Turco AE, Abler LL, Sandhu SK, Cadena MT, Malladi VS *et al* (2020) Urethral luminal epithelia are castration-insensitive cells of the proximal prostate. *Prostate* 80: 872 – 884

Karthaus W, Iaquinta P, Drost J, Gracanin A, van Boxtel R, Wongvipat J, Dowling C, Gao D, Begthel H, Sachs N *et al* (2014) Identification of multipotent luminal progenitor cells in human prostate organoid cultures. *Cell* 159: 163 – 175

Karthaus WR, Hofree M, Choi D, Linton EL, Turkekul M, Bejnood A, Carver B, Gopalan A, Abida W, Laudone V *et al* (2020) Regenerative potential of prostate luminal cells revealed by single-cell analysis. *Science* 368: 497 – 505

Kirby RS, Lowe D, Bultitude MI, Shuttleworth KE (1982) Intra-prostatic urinary reflux: an aetiological factor in abacterial prostatitis. *Br J Urol* 54: 729 – 731

Krausgruber T, Fortelny N, Fife-Gernedl V, Senekowitsch M, Schuster LC, Lercher A, Nemc A, Schmidl C, Rendeiro AF, Bergthaler A *et al* (2020) Structural cells are key regulators of organ-specific immune responses. *Nature* 583: 296 – 302

Kretzschmar K, Clevers H (2016) Organoids: modeling development and the stem cell niche in a dish. *Dev Cell* 38: 590 – 600

Kwon O-J, Zhang L, Ittmann MM, Xin L (2014) Prostatic inflammation enhances basal-to-luminal differentiation and accelerates initiation of prostate cancer with a basal cell origin. *Proc Natl Acad Sci USA* 111: E592 – E600

Kwon O-J, Zhang B, Zhang L, Xin L (2016a) High fat diet promotes prostatic basal-to-luminal differentiation and accelerates initiation of prostate epithelial hyperplasia originated from basal cells. *Stem Cell Res* 16: 682 – 691

Kwon O-J, Zhang L, Xin L (2016b) Stem cell antigen-1 identifies a distinct androgen-independent murine prostatic luminal cell lineage with bipotent potential. *Stem Cells* 34: 191 – 202

Kwon O-J, Choi JM, Zhang LI, Jia D, Wei X, Li Z, Zhang Y, Jung SY, Creighton CJ, Xin LI (2020) The Sca-1+ and Sca-1- mouse prostatic luminal cell lineages are independently sustained. *Stem Cells* 38: 1479 – 1491

Li J, Xu C, Lee HJ, Ren S, Zi X, Zhang Z, Wang H, Yu Y, Yang C, Gao X *et al* (2020) A genomic and epigenomic atlas of prostate cancer in Asian populations. *Nature* 580: 93 – 99

Love MI, Huber W, Anders S (2014) Moderated estimation of fold change and dispersion for RNA-seq data with DESeq2. *Genome Biol* 15: 550

Lu X, Jin E-J, Cheng XI, Feng S, Shang X, Deng P, Jiang S, Chang Q, Rahmy S, Chaudhary S *et al* (2017) Opposing roles of TGFβ and BMP signaling in prostate cancer development. *Genes Dev* 31: 2337 – 2342

Massagué J (2012) TGFβ signalling in context. *Nat Rev Mol Cell Biol* 13: 616 – 630

McKeehan WL, Adams PS (1988) Heparin-binding growth factor/prostatropin attenuates inhibition of rat prostate tumor epithelial cell growth by transforming growth factor type beta. *In Vitro Cell Dev Biol* 24: 243 – 246

Mevel R, Steiner I, Mason S, Galbraith LCA, Patel R, Fadlullah MZH, Ahmad I, Leung HY, Oliveira P, Blyth K *et al* (2020) RUNX1 marks a luminal castration-resistant lineage established at the onset of prostate development. *Elife* 9: e60225

Moses HL, Roberts AB, Derynck R (2016) The discovery and early days of TGF-β: a historical perspective. *Cold Spring Harb Perspect Biol* 8: a021865

Nakai Y, Nelson WG, De Marzo AM (2007) The dietary charred meat carcinogen 2-amino-1-methyl-6-phenylimidazo[4,5-b]pyridine acts as both a tumor initiator and promoter in the rat ventral prostate. *Cancer Res* 67: 1378 – 1384

Nakamura T, Takio K, Eto Y, Shibai H, Titani K, Sugino H (1990) Activin-binding protein from rat ovary is follistatin. *Science* 247: 836 – 838

Nieri D, Berardinelli F, Sgura A, Cherubini R, De Nadal V, Gerardi S, Tanzarella C, Antoccia A (2013) Cyogenetics effects in AG01522 human primary fibroblasts exposed to low doses of radiations with different quality. *Int J Radiat Biol* 89: 698 – 707

Ørsted DD, Bojesen SE (2013) The link between benign prostatic hyperplasia and prostate cancer. *Nat Rev Urol* 10: 49 – 54

Oshimori N, Oristian D, Fuchs E (2015) TGF-β promotes heterogeneity and drug resistance in squamous cell carcinoma. *Cell* 160: 963 – 976

Paull EO, Aytes A, Jones SJ, Subramaniam PS, Giorgi FM, Douglass EF, Tagore S, Chu B, Vasciaveo A, Zheng S *et al* (2021) A modular master regulator landscape controls cancer transcriptional identity. *Cell* 184: 334 – 351.e20

Pignon J-C, Grisanzio C, Carvo I, Werner L, Regan M, Wilson EL, Signoretti S (2015) Cell kinetic studies fail to identify sequentially proliferating progenitors as the major source of epithelial renewal in the adult murine prostate. *PLoS One* 10: e0128489

Platanias LC (2005) Mechanisms of type-I- and type-II-interferon-mediated signalling. *Nat Rev Immunol* 5: 375 – 386

Quinn DI, Sandler HM, Horvath LG, Goldkorn A, Eastham JA (2017) The evolution of chemotherapy for the treatment of prostate cancer. *Ann Oncol* 28: 2658 – 2669

Rappsilber J, Mann M, Ishihama Y (2007) Protocol for micro-purification, enrichment, pre-fractionation and storage of peptides for proteomics using StageTips. *Nat Protoc* 2: 1896 – 1906

Rodgarkia-Dara C, Vejda S, Erlach N, Losert A, Bursch W, Berger W, Schulte-Hermann R, Grusch M (2006) The activin axis in liver biology and disease. *Mutat Res* 613: 123 – 137

Rueden CT, Schindelin J, Hiner MC, DeZonia BE, Walter AE, Arena ET, Eliceiri KW (2017) Image J2: ImageJ for the next generation of scientific image data. *BMC Bioinformatics* 18: 529

Salm SN, Burger PE, Coetzee S, Goto K, Moscatelli D, Wilson EL (2005) TGF-{beta} maintains dormancy of prostatic stem cells in the proximal region of ducts. *J Cell Biol* 170: 81 – 90

Samper E, Goytisolo FA, Slijepcevic P, van Buul PP, Blasco MA (2000) Mammalian Ku86 protein prevents telomeric fusions independently of the length of TTAGGG repeats and the G-strand overhang. *EMBO Rep* 1: 244 – 252

Sato S, Sanjo H, Takeda K, Ninomiya-Tsuji J, Yamamoto M, Kawai T, Matsumoto K, Takeuchi O, Akira S (2005) Essential function for the kinase TAK1 in innate and adaptive immune responses. *Nat Immunol* 6: 1087 – 1095

Sfanos KS, Yegnasubramanian S, Nelson WG, De Marzo AM (2018) The inflammatory microenvironment and microbiome in prostate cancer development. *Nat Rev Urol* 15: 11 – 24

Shim J-H, Xiao C, Paschal AE, Bailey ST, Rao P, Hayden MS, Lee K-Y, Bussey C, Steckel M, Tanaka N *et al* (2005) TAK1, but not TAB1 or TAB2, plays an essential role in multiple signaling pathways in vivo. *Genes Dev* 19: 2668 – 2681

Shinohara DB, Vaghasia AM, Yu S-H, Mak TN, Brüggemann H, Nelson WG, De Marzo AM, Yegnasubramanian S, Sfanos KS (2013) A mouse model of chronic prostatic inflammation using a human prostate cancer-derived isolate of Propionibacterium acnes. *Prostate* 73: 1007 – 1015

Simons BW, Durham NM, Bruno TC, Grosso JF, Schaeffer AJ, Ross AE, Hurley PJ, Berman DM, Drake CG, Thumbikat P *et al* (2015) A human prostatic bacterial isolate alters the prostatic microenvironment and accelerates prostate cancer progression. *J Pathol* 235: 478 – 489

Sneddon JB, Zhen HH, Montgomery K, van de Rijn M, Tward AD, West R, Gladstone H, Chang HY, Morganroth GS, Oro AE *et al* (2006) Bone morphogenetic protein antagonist gremlin 1 is widely expressed by cancer-associated stromal cells and can promote tumor cell proliferation. *Proc Natl Acad Sci USA* 103: 14842 – 14847

Sorrentino A, Thakur N, Grimsby S, Marcusson A, von Bulow V, Schuster N, Zhang S, Heldin C-H, Landström M (2008) The type I TGF-beta receptor engages TRAF6 to activate TAK1 in a receptor kinase-independent manner. *Nat Cell Biol* 10: 1199 – 1207

Sporn MB, Todaro GJ (1980) Autocrine secretion and malignant transformation of cells. *N Engl J Med* 303: 878 – 880

Tarragona M, Pavlovic M, Arnal-Estapé A, Urosevic J, Morales M, Guiu M, Planet E, González-Suárez E, Gomis RR (2012) Identification of NOG as a specific breast cancer bone metastasis-supporting gene. *J Biol Chem* 287: 21346 – 21355

Toivanen R, Shen MM (2017) Prostate organogenesis: tissue induction, hormonal regulation and cell type specification. *Development* 144: 1382 – 1398

Tucker RF, Shipley GD, Moses HL, Holley RW (1984) Growth inhibitor from BSC-1 cells closely related to platelet type beta transforming growth factor. *Science* 226: 705 – 707

Vergote I, Heitz F, Buderath P, Powell M, Sehouli J, Lee CM, Hamilton A, Fiorica J, Moore KN, Teneriello M *et al* (2020) A randomized, double-blind, placebo-controlled phase 1b/2 study of ralimetinib, a p38 MAPK inhibitor, plus gemcitabine and carboplatin versus gemcitabine and carboplatin for women with recurrent platinum-sensitive ovarian cancer. *Gynecol Oncol* 156: 23 – 31

Wang Z, Hu L, Salari K, Bechis SK, Ge R, Wu S, Rassoulian C, Pham J, Wu C-L, Tabatabaei S *et al* (2017) Androgenic to oestrogenic switch in the human adult prostate gland is regulated by epigenetic silencing of steroid 5α-reductase 2. *J Pathol* 243: 457 – 467

Washino S, Rider LC, Romero L, Jillson LK, Affandi T, Ohm AM, Lam ET, Reyland ME, Costello JC, Cramer SD (2019) Loss of MAP3K7 sensitizes prostate cancer cells to CDK1/2 inhibition and DNA damage by disrupting homologous recombination. *Mol Cancer Res* 17: 1985 – 1998

Wei X, Zhang LI, Zhou Z, Kwon O-J, Zhang Y, Nguyen H, Dumpit R, True L, Nelson P, Dong B *et al* (2019) Spatially restricted stromal wnt signaling restrains prostate epithelial progenitor growth through direct and indirect mechanisms. *Cell Stem Cell* 24: 753 – 768.e6

Yaeger R, Chatila WK, Lipsyc MD, Hechtman JF, Cercek A, Sanchez-Vega F, Jayakumaran G, Middha S, Zehir A, Donoghue MTA *et al* (2018) Clinical sequencing defines the genomic landscape of metastatic colorectal cancer. *Cancer Cell* 33: 125 – 136.e3

Yamaguchi K, Shirakabe K, Shibuya H, Irie K, Oishi I, Ueno N, Taniguchi T, Nishida E, Matsumoto K (1995) Identification of a member of the MAPKKK family as a potential mediator of TGF-beta signal transduction. *Science* 270: 2008 – 2011

Zhang B, Kwon O-J, Henry G, Malewska A, Wei X, Zhang LI, Brinkley W, Zhang Y, Castro P, Titus M *et al* (2016) Non-cell-autonomous regulation of prostate epithelial homeostasis by androgen receptor. *Mol Cell* 63: 976 – 989